nature communications

Article

https://doi.org/10.1038/s41467-025-61522-6

Multi-stimulated far-UVC luminescence for solar-blind imaging

Received: 17 December 2024

Accepted: 24 June 2025

Published online: 06 July 2025

Check for updates

Chongyang Cai[1], Leipeng Li[1] ✉, Xiaohuan Lv[1], Huimin Li[1], Tao Li[1], Pei Li[1], Wenting Zhao[1], Lingzhu Zi[1], Shiji Feng[1], Xuan Fan[1], Hailei Zhang[2], Dengfeng Peng[3,4,5] ✉, Feng Wang[6,7] ✉, Jianrong Qiu[8] & Yanmin Yang[1] ✉

Lanthanides-doped luminescent materials have gathered considerable attention due to their application potential in stress sensing, lighting and display, anti-counterfeiting technology and so forth. However, existing materials mainly cover the 380–1540 nm range, with slight extension to the UV region, impeding their applications in solar-blind imaging, background-free tracking, concealed communication, etc. To address this challenge, here we propose guidelines for far-UVC (200–230 nm) optical design. Accordingly, we achieve multi-stimulated far-UVC luminescence at ~222 nm in Pr^{3+}-doped SrF_2, stemming from the inter-configurational $4f5d \rightarrow 4f^2$ transition of Pr^{3+}. Besides Pr^{3+}, the SrF_2 host shows high tolerance to Ce^{3+}, Nd^{3+}, Sm^{3+}, $Eu^{2+,3+}$, Gd^{3+}, Tb^{3+}, Dy^{3+}, Ho^{3+}, Er^{3+}, Tm^{3+} and Yb^{3+}, vastly extending the emission wavelength across the entire spectral range from 200 to 1700 nm. Particularly, these materials exhibit self-recoverable mechanoluminescence by direct mechanical excitation, along with thermally and mechanically stimulated emission after X-ray irradiation. We demonstrate that these lanthanides-doped SrF_2 crystals offer unique opportunities for high-contrast marking and structural health monitoring in complex environments.

Luminescent materials play a crucial role in modern technology and everyday life[1–4]. Scientists are actively developing high-performance luminescent materials capable of emitting multi-mode luminescence, including electroluminescence, photoluminescence (PL), cathodoluminescence, thermoluminescence (TL), mechanoluminescence (ML) and so forth[5–11]. ML materials are of particular interest due to their ability to convert mechanical energy from actions like compression, stretching and friction into light. Based on direct mechanical excitation and mechanically stimulated processes, these ML materials have enabled a wide range of applications, showcasing substantial potential for technological advancement and sustainable energy utilization. Such "trash to treasure" feature makes ML materials attract ever-increasing attention, especially considering that the global energy crisis is intensifying nowadays[12–14].

ML has been observed in both organic and inorganic systems[15–19]. Compared to their organic counterparts, inorganic ML materials stand out due to excellent physicochemical stability and repeatability and have been used for self-powered sensors, security marking, imaging

[1]College of Physics Science and Technology, Hebei University, Baoding, China. [2]College of Chemistry & Materials Science, Hebei University, Baoding, China. [3]Shenzhen Key Laboratory of Intelligent Optical Measurement and Detection, Shenzhen University, Shenzhen, China. [4]Key Laboratory of Optoelectronic Devices and Systems of Ministry of Education and Guangdong Province, College of Physics and Optoelectronic Engineering, Shenzhen University, Shenzhen, China. [5]State Key Laboratory of Radio Frequency Heterogeneous Integration, Shenzhen University, Shenzhen, China. [6]Department of Materials Science and Engineering, City University of Hong Kong, Hong Kong SAR, China. [7]Hong Kong Institute for Clean Energy, City University of Hong Kong, Hong Kong SAR, China. [8]State Key Laboratory of Modern Optical Instrumentation, College of Optical Science and Engineering, Zhejiang University, Hangzhou, China. ✉e-mail: lpl@hbu.edu.cn; pengdengfeng@szu.edu.cn; fwang24@cityu.edu.hk; yangym@hbu.edu.cn

and structural monitoring[20–27]. Although ML has a long history of over four hundred years, it has only collected considerable attention since 1999, when Xu's group first reported elastic ML in $SrAl_2O_4:Eu^{2+}$ and $ZnS:Mn^{2+}$ [28,29]. One of the most important parameters for ML is wavelength, as it directly determines specific applications. To expand available ML wavelengths, several strategies are proposed, including searching for new hosts and luminescent centers, introducing energy transfer, engineering host lattice and constructing organic/inorganic hybrid[30–36]. Among these efforts, scientists mainly focus on the visible and near-infrared regions, with little attention to the UV range[37,38]. By doping Pr^{3+}, Nd^{3+}, Sm^{3+}, Eu^{3+}, Tb^{3+}, Dy^{3+}, Er^{3+}, Ho^{3+}, Tm^{3+} and Yb^{3+} ions into CaZnOS, for example, Wang's group achieved ML wavelength coverage in the 380–1030 nm range[39]. Subsequently, Peng's group extended the ML wavelength to 1540 nm by leveraging the $^4I_{13/2} \rightarrow {}^4I_{15/2}$ transition of Er^{3+} in CaZnOS[40]. Therefore, by carefully doping different lanthanides or lanthanide pairs in single CaZnOS, the ML can be tuned over the 380–1540 nm range (Supplementary Fig. 1 and Table 1). This raises the question of how broad the wavelength range of ML can reach in a single host.

In the longwave band boundary, the intra-configurational 4f level dominantly determines the emission wavelength, making the answer rather clear[41,42]. In the shortwave limit, however, it is filled with unknowns. Reports on ultraviolet-C (UVC, 200–280 nm) and ultraviolet-B (UVB, 280–320 nm) ML are quite limited. In 2023, Wang's team observed UVB ML from $Y_3Al_2Ga_3O_{12}:Gd^{3+}$ with a central wavelength at 313 nm, which was attributed to the $^6P_{7/2} \rightarrow {}^8S_{7/2}$ transition of Gd^{3+} [43]. In the same year, our group collected the $^1I_6 \rightarrow {}^3H_6$ transition of Tm^{3+} in MgF_2 in the ML mode, peaking at 292 nm[44]. Using a trial-and-error method, we also observed ML at 250 nm in $NaYF_4:Pr^{3+}$ (Pr^{3+}:$^1S_0 \rightarrow {}^3F_4$) and 230 nm in $Sr_2P_2O_7:Pr^{3+}$ (Pr^{3+}:5 d → 4 f)[45,46]. These observations inspire us to break the shortwave limit in far-UVC (200–230 nm) using Pr^{3+} dopants by refining the host lattice. The ultra-shortwave emissions are expected to expand the applications of ML, such as in micropollutant degradation, inactivation of bacteria, concealed communication, and particularly in solar-blind imaging[47,48]. Solar-blind imaging represents a pivotal advancement in remote sensing and optical detection methodologies, emphasizing the importance of detecting UVC radiation in the absence of solar interference. By operating in a solar-blind region, imaging systems can effectively filter out the overwhelming background noise generated by sunlight and artificial light sources, allowing for enhanced visibility of faint signals from targets or phenomena of interest. Consequently, solar-blind imaging is particularly valuable for applications such as military surveillance, atmospheric research and pollution monitoring, where conventional imaging systems may struggle.

To establish general guidelines for far-UVC ML design, we herein analyze the complicated situation of Pr^{3+} energy levels under the influence of host matrices. Accordingly, we develop a class of Pr^{3+}-doped SrF_2 crystals and realize far-UVC ML with central wavelength at approximately 222 nm through the $4f5d \rightarrow {}^3H_4$ transition of Pr^{3+}. Moreover, we confirm that the SrF_2 hosts show high tolerance to various lanthanides as luminescent centers, including Ce^{3+}, Nd^{3+}, Sm^{3+}, $Eu^{2+,3+}$, Gd^{3+}, Tb^{3+}, Dy^{3+}, Ho^{3+}, Er^{3+}, Tm^{3+} and Yb^{3+}. The ML of these samples covers nearly the whole spectral range from 200 to 1700 nm, superior to the previous reports (Supplementary Fig. 1 and Table 1). Taking into account the fact that the UVC part of the solar spectrum has been totally absorbed by the ozone sphere and UVC light is invisible to the naked eyes, we demonstrate the potential application of $SrF_2:Pr^{3+}$ for high-contrast and background-free marking. In addition, we also show how to use the multi-bands of ML for encryption, anti-counterfeiting, non-destructive testing and structural health monitoring.

Results

Design principles for far-UVC emission

In order to obtain far-UVC ML in Pr^{3+} ions, a set of conditions should be satisfied (Fig. 1). At the most basic level, the bandgap of the host where Pr^{3+} ions are embedded should be greater than 6.2 eV (≈200 nm), such that the far-UVC photons are not absorbed by the host (Fig. 1, step 1). This requirement excludes a large portion of semiconductors and oxysalts, such as sulfide (ZnS:3.5 ~ 3.8 eV, CaS:3.06 eV), oxides (Y_2O_3:5.5 eV, ZnO:3.37 eV and $BaTiO_3$:3.3 eV), tungstates ($CaWO_4$:4.5 eV) and molybdates ($CaMoO_4$:3.7 eV), despite their popularity in hosting visible emitting ions.

Next, we pay attention to the $^1S_0$ state of Pr^{3+}, which may generate far-UVC emissions through the $^1S_0 \rightarrow {}^3H_4$ (≈215 nm) and $^1S_0 \rightarrow {}^3H_5$ (≈225 nm) transitions (Fig. 1, step 2). It should be noted, however, that the emission intensities of these intra-configurational transitions are very weak due to their parity-forbidden nature. Another downside is that the total transition branching ratios of $^1S_0 \rightarrow {}^3H_{4,5}$ are usually less than 1%. More than 60% ~ 80% of the excited $^1S_0$ state terminates in the lower-lying $^1I_6$ state, peaking at ≈400 nm[49,50]. This explains why the $^1S_0 \rightarrow {}^3H_4$ (≈215 nm) and $^1S_0 \rightarrow {}^3H_5$ (≈225 nm) transitions are hardly observed in most reports. Even if they are observed under optimal conditions, the emission intensity is too weak[51,52].

The above discussions suggest that the $^1S_0$ state is unfavorable to far-UVC emissions. Therefore, it is more advisable to expect far-UVC emissions from the 4f5d state. The longwave boundary of far-UVC is at 230 nm, corresponding to ≈43478 cm^{-1}. Accordingly, the lower limit of the 4f5d state should be above 43478 cm^{-1} (Fig. 1, step 3). Under this premise constraint, the energy position of the 4f5d state should be as close as possible to the center wavelength (≈46500 cm^{-1}) of far-UVC, ensuring that most emissions fall within the far-UVC range.

Notably, an over-high energy of the 4f5d should also be avoided. Otherwise, the excited electrons at the 4f5d state will be non-radiatively relaxed to the lower $^1S_0$ state, followed by the emissions from the $^1S_0$ state (Fig. 1, step 4). In $SrAl_{12}O_{19}:Pr^{3+}$, for example, the lowest 4f5d state and $^1S_0$ state were ≈47600 cm^{-1} and ≈46500 cm^{-1}, respectively, with an energy difference of 1100 cm^{-1} [53]. In this compound, only weak transitions from the $^1S_0$ state were observed over the

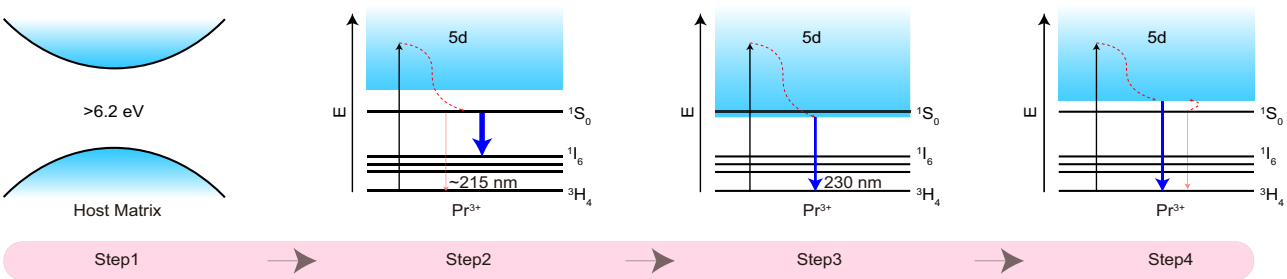

Fig. 1 | Design principles for far-UVC emission. Step 1: Calculation of the band gap of the host crystal. Step 2: Assessment of the position and intensity of transitions from the $^1S_0$ state of Pr^{3+}. Step 3: Determine the lowest energy 4f5d state for the longwave boundary of far-UVC emission. Step 4: Analysis of the situation in which the transitions from the 4f5d state of Pr^{3+} dominate the emissions as well as the shortwave boundary of far-UVC emission.

far-UVC region at 220 nm. In contrast, the lowest 4f5d state in $LaB_3O_6:Pr^{3+}$ is higher than the $^1S_0$ state by ≈900 cm^{-1}, and the 5d → 4f transitions dominated the emission spectrum in the far-UVC range due to the Boltzmann distribution between the $^1S_0$ state and the upper 4f5d state[54]. Combining the above two situations, we suggest that the position of the 4f5d state should not be higher than that of the $^1S_0$ state by 1000 cm^{-1}.

Summarizing all the information above, we can draw the following semi-empirical conclusion: the 4f5d state of Pr^{3+} should be in the range of 43478 to 47500 cm^{-1}. Considering that the position of the $^1S_0$ state may slightly change with the alteration of the host (<500 cm^{-1}), the upper energy limit of the 4f5d state of Pr^{3+} can be appropriately relaxed to ≈48000 cm^{-1}. Additionally, it is important to note that the host material where Pr^{3+} ions are embedded needs to have good far-UVC transmission. This clue points to fluorides that typically possess a wide band gap and good ultraviolet transmittance. Based on previous reports, the 4f → 5d transition of Pr^{3+} in SrF_2 had an absorption peak at ≈46600 cm^{-1} [55]. Such energy value well satisfies the above guidelines, thus making it possible to achieve far-UVC ML. Therefore, $SrF_2:Pr^{3+}$ was chosen as a representative for examination in the subsequent sections.

Material synthesis and characterization

A series of $SrF_2:x\%Pr^{3+}$ (x = 0.1, 0.2, 0.5, 0.7, and 1) phosphors were synthesized by a high-temperature solid-state technique. The X-ray diffraction (XRD) patterns of these samples, mainly comprising the diffraction peaks of (1 1 1), (2 0 0), (2 2 0), (3 1 1), (4 0 0), and (3 3 1) planes, matched well with cubic phase SrF_2 crystals (PDF#88-2294) (Fig. 2a). It suggested that $SrF_2:Pr^{3+}$ crystalized in the single center-symmetric structure with the *Fm*-3*m* space group (Fig. 2b). In this structure, Sr ions occupied an octahedral coordination environment, where each Sr ion was surrounded by eight F ions. Meanwhile, Pr^{3+} ions entered the host lattice by substituting the Sr^{2+} sites (Supplementary Table 2), which was confirmed by the Rietveld refinement analysis (Fig. 2c and Supplementary Table 3).

The scanning electron microscopy (SEM) image revealed an irregular morphology of the as-synthesized $SrF_2:Pr^{3+}$ in the micrometer length scale, with Sr, F and Pr elements distributed uniformly at the single particle level (Fig. 2d and Supplementary Fig. 2). The energy dispersive spectroscopy (EDS) results proved that the element ratios of Sr, F, and Pr were as expected (Supplementary Figs. 3–7). The X-ray photoelectron spectroscopy (XPS) results further validated the presence of constituent elements (Fig. 2e). The XPS peaks centered approximately at 966 and 946 eV were not observed, indicating the absence of tetravalent Pr. The peaks at the binding energy of 931.9 and 935.3 eV were ascribed to trivalent Pr. We also measured the Raman shift of $SrF_2:0.5\%Pr^{3+}$ (Supplementary Fig. 8). A prominent band appeared at approximately 285 cm^{-1}, attributed to the first-order F_{2g} mode of SrF_2[56]. The selected area electron diffraction (SAED) exhibited sharp diffraction spots with a periodic arrangement, demonstrating good crystallinity (Fig. 2f). The high-resolution transmission electron microscopy (HR-TEM) images further disclosed the good crystallinity of our samples, which show well-defined (2 0 0) and (1 1 1) lattice fringes with observed *d*-spacings of 0.290 and 0.335 nm, respectively (Fig. 2g and Supplementary Fig. 9).

Multi-stimulated far-UVC luminescence

We designed a set of experimental procedures to systematically investigate the multi-stimulated luminescence, as schematically shown in Fig. 3a. Figure 3b depicts the emission spectra of $SrF_2:Pr^{3+}$ under different conditions. As can be seen, the sample can be directly excited by mechanical action through the self-recoverable ML mechanism (Stage I). After being exposed to X-ray irradiation, bright persistent

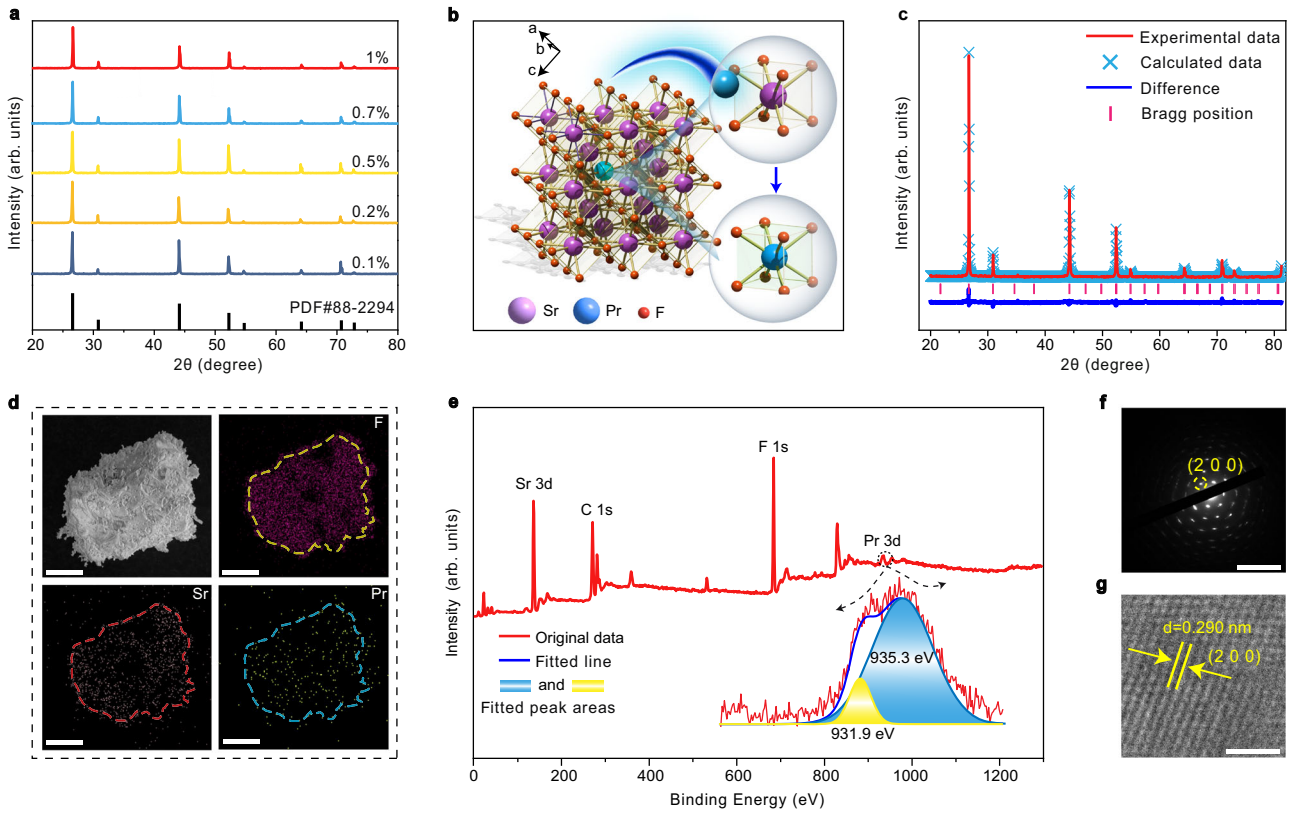

Fig. 2 | Characterization of $SrF_2:Pr^{3+}$. **a** X-ray diffraction patterns of $SrF_2:x\%Pr^{3+}$ (x = 0.1, 0.2, 0.5, 0.7, and 1). **b** Crystal structure of $SrF_2:Pr^{3+}$. **c** Rietveld structure refinements of $SrF_2:0.5\%Pr^{3+}$. **d** Scanning electron microscopy and elemental mapping images $SrF_2:0.5\%Pr^{3+}$ (scale bar: 50 μm). **e** X-ray photoelectron spectroscopy profile of $SrF_2:0.5\%Pr^{3+}$. **f** Selected area electron diffraction image of $SrF_2:0.5\%Pr^{3+}$ (scale bar: 10 nm^{-1}). **g** High-resolution transmission electron microscopy image of $SrF_2:0.5\%Pr^{3+}$ (scale bar: 2 nm). Source data are provided as a Source Data file.

https://doi.org/10.1038/s41467-025-61522-6

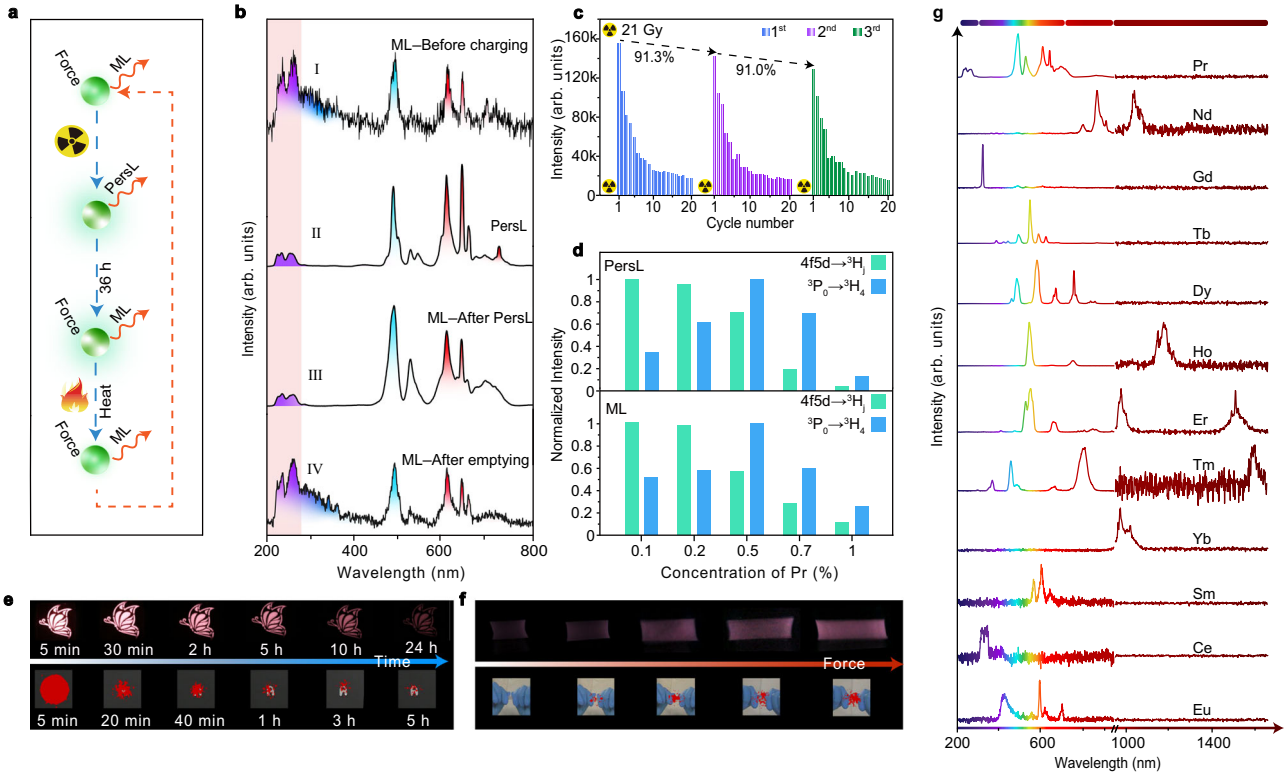

Fig. 3 | Optical properties of SrF_2:Pr^{3+}. **a** Schematic of experimental procedures for mechanoluminescence (ML) and persistent luminescence (PersL) measurement. **b** Comparison of spectra of SrF_2:0.5%Pr^{3+} under different conditions. Stage I: obtained before X-ray irradiation. Stage II: obtained immediately after stoppage of 5-min X-ray irradiation. Stage III: obtained upon force stimulation at 5 N after PersL. Stage IV: obtained after thermal bleach. **c** Repeatability results of trap-controlled ML. **d** PersL and ML intensity of SrF_2:Pr^{3+} as a function of Pr^{3+} content. **e** Photographs of visible and UVC PersL of SrF_2:0.5%Pr^{3+}, showing progressive changes over time following a 5-min X-ray irradiation. **f** Photographs of visible and UVC ML of SrF_2:0.5%Pr^{3+}@polydimethylsiloxane films stretched under different magnitudes of force. **g** ML spectra of SrF_2 singly doped with different lanthanides (0.5%mol). Source data are provided as a Source Data file.

luminescence (PersL) was detected (Stage II), indicating the occurrence of charge carrier trapping. Following PersL, we further detected trap-controlled ML by application of force (Stage III). The trap-controlled ML was about 90-fold stronger than the self-recoverable ML, and the intensity fell back to the original level by thermal cleaning of the trap states (Stage IV). Notably, all the spectra are dominated by the characteristic emission peaks of Pr^{3+} ions, suggesting that Pr^{3+} ions consistently acted as luminescent centers during the whole process (Fig. 3b). Specifically, the visible emission bands are attributed to the $^3P_0 \rightarrow {}^3H_4$ (488 nm), $^3P_1 \rightarrow {}^3H_5$ (524 nm), $^3P_0 \rightarrow {}^3H_6$ (606 nm) /$^1D_2 \rightarrow {}^3H_4$ (606 nm) and $^3P_0 \rightarrow {}^3F_2$ (640 nm) transitions of Pr^{3+}. The UVC emission bands are assigned as the 4f5d → $^3H_4$ (222 nm), 4f5d → $^3H_5$ (233 nm) and 4f5d → $^3H_6$ (259 nm) transitions of Pr^{3+}. Note that the broad band peaking at 300 nm came from the self-trapped exciton of the host (Supplementary Fig. 10)[57–59]. The presence of the ML line at 222 nm proves the reliability of our guidelines for designing far-UVC luminescence.

We next examined the repeatability of ML. Both the self-recoverable and trap-controlled ML decreased after several cycles of continuous operation (Fig. 3c and Supplementary Fig. 11). This phenomenon was also previously observed by several groups[13,15,22,25,43]. By checking the XRD results of SrF_2:0.5%Pr^{3+} after grinding, we found no noticeable change in the crystal structure (Supplementary Fig. 12). The comparison of SEM images of SrF_2:Pr^{3+} before and after grinding suggested that the samples became progressively finer (Supplementary Fig. 13). As the surface area and morphology of samples had been modified, it was reasonable to assume that the ML property, including both self-recoverable and trap-controlled ML, were affected to some extent[60].

We optimized the content of Pr^{3+} in SrF_2 with emphasis on the 4f5d → $^3H_{4,5,6}$ and $^3P_0 \rightarrow {}^3H_4$ transitions. The transitions from the 4f5d and $^3P_0$ states exhibit opposite trends with doping concentration (Fig. 3d and Supplementary Fig. 14). Such discrepancy is explained by the possible cross-relaxation-induced concentration quenching mechanism (Supplementary Fig. 15). With gradually increasing the content of Pr^{3+}, the 4f5d → $^3H_{4,5,6}$ transition showed a monotonic decrease trend, as the [4f5d → $^3P_{0,1}$]/[$^1D_2 \leftarrow {}^3H_4$] cross-relaxation process was harmful to the 4f5d state. By contrast, the $^3P_0 \rightarrow {}^3H_4$ transition increased first over the range of $0.1 < x < 0.5$ because the [4f5d → $^3P_{0,1}$]/[$^1D_2 \leftarrow {}^3H_4$] cross-relaxation would populate the $^3P_0$ state, together with the increment of luminescent centers. When the content of Pr^{3+} exceeded 0.5%, the $^3P_0 \rightarrow {}^3H_4$ transition experienced a continuous decline, attributed to the predominance of [$^3P_{0,1} \rightarrow {}^1G_4$]/[$^1G_4 \leftarrow {}^3H_4$] cross-relaxation[59].

Under a doping concentration of 0.5%, the SrF_2:Pr^{3+} exhibited pronounced and balanced visible and UVC PersL after the stoppage of X-ray irradiation (Fig. 3e and Supplementary Fig. 16). It was easy to distinguish the UVC PersL signal from the background noise after several hours. Even after one day, the visible PersL was observed clearly. Over the whole PersL process, the positions of emission spectra remained unchanged (Supplementary Fig. 17). After the release of room temperature PersL, SrF_2:Pr^{3+} continued to emit in the visible and UVC regions by mechanical stimulation (Fig. 3f and Supplementary Movie 1). With increasing the force, both the UVC and visible ML were enhanced. Notably, the ML intensity of $^3P_0 \rightarrow {}^3H_4$ (488 nm) and 4f5d → $^3H_{4,5,6}$ transitions displayed different responses to the external force (Supplementary Figs. 18 and 19), pushing us to establish a ratiometric method for stress sensing[61,62]. The ML intensity ratio between the $^3P_0 \rightarrow {}^3H_4$ and 4f5d → $^3H_{4,5,6}$ transitions presented a monotonic decrease by raising the force, with the relative sensitivity varying from 3% N^{-1} to 7% N^{-1} over the 5–25 N range (Supplementary Fig. 20).

https://doi.org/10.1038/s41467-025-61522-6

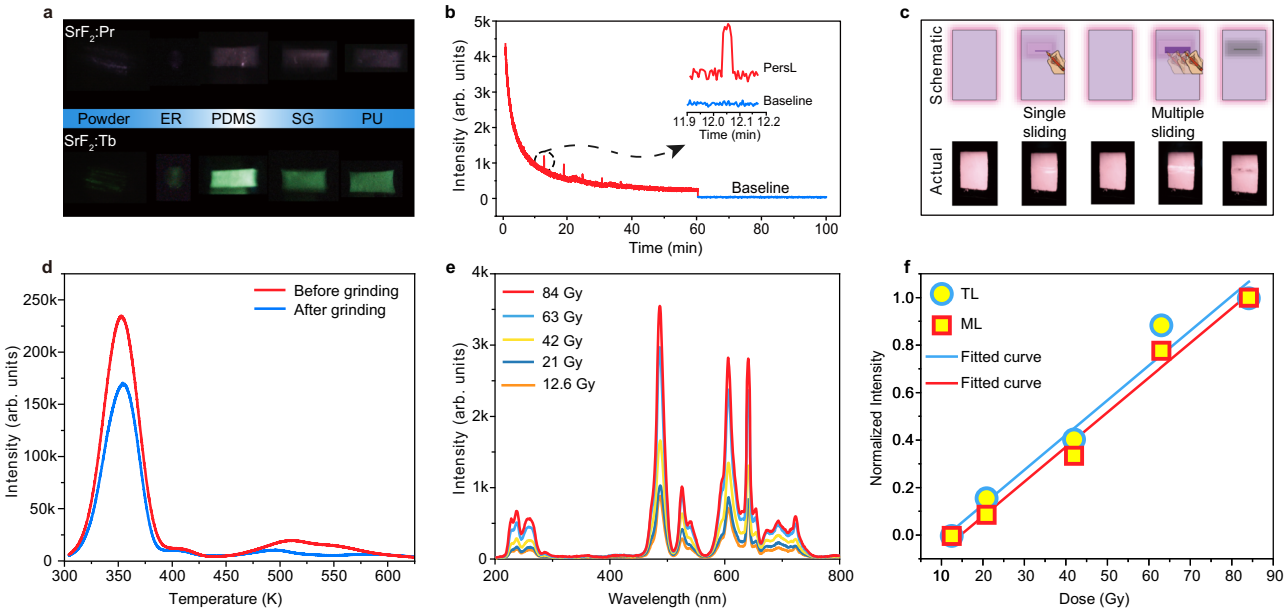

Fig. 4 | Mechanistic study of SrF_2:Pr^{3+}. **a** Photographs of SrF_2:0.5%Pr^{3+} powder and SrF_2:0.5%Pr^{3+} embedded in different polymers, including epoxy resin (ER), polydimethylsiloxane (PDMS), silicon gel (SG) and polyurethane (PU), under mechanical action. **b** Persistent luminescence (PersL) decay curve of SrF_2:0.5%Pr^{3+} after stoppage of 5-min X-ray irradiation. Inset: enlarged PersL signal upon stimulation of external force. **c** Photographs of SrF_2:0.5%Pr^{3+} upon single- and multiple-sliding during the PersL process. **d** Thermoluminescence (TL) curves of SrF_2:0.5%Pr^{3+} before and after grinding for 20 min. **e** Mechanoluminescence (ML) spectra of SrF_2:0.5%Pr^{3+} after different X-ray exposure dose. **f** Normalized TL and ML intensities of SrF_2:0.5%Pr^{3+} as a function of X-ray irradiation dose. Source data are provided as a Source Data file.

We also prepared a series of SrF_2 samples doped with various lanthanides (Ce^{3+}, Nd^{3+}, Sm^{3+}, $Eu^{2+,3+}$, Gd^{3+}, Tb^{3+}, Dy^{3+}, Ho^{3+}, Er^{3+}, Tm^{3+}, and Yb^{3+}) to expand the spectral range. The XRD and XPS results proved the successful preparation of target materials (Supplementary Figs. 21 and 22). All these samples emitted self-recoverable ML (Supplementary Figs. 23 and 24). After being pre-charged by X-ray, these samples emitted tunable PersL due to characteristic transitions in relevant lanthanide dopants (Supplementary Figs. 25–27). After the PersL faded out in one and a half days, all samples presented trap-controlled ML, nearly covering the whole spectral range from 200 to 1700 nm (Fig. 3g and Supplementary Figs. 28–31).

Mechanistic investigation of multi-stimulated emission

The self-recoverable ML was previously observed in some asymmetric materials like CaZnOS:Mn^{2+} and ZnS:Mn^{2+} due to piezoelectricity[28,63]. Accordingly, we conducted the piezoresponse force microscopy (PFM) tests to check the piezoelectric effect. Pure SrF_2 did not show any piezoelectric properties due to the centrosymmetric nature (Supplementary Fig. 32). Nevertheless, piezoelectric hysteresis and butterfly loops appeared for SrF_2:Pr^{3+} during the PFM measurements, indicating that the introduction of Pr^{3+} disrupted the local symmetry of SrF_2 and thereby endowed SrF_2:Pr^{3+} with local piezoelectric properties (Supplementary Fig. 33). The PFM results verify the arise of piezoelectric potential in the ML process.

It should be noted that, in addition to the piezoelectric effect, triboelectrification has recently been considered as another key mechanism for ML. A notable feature of triboelectrification-induced ML is that the ML intensity exhibits a strong dependence on the triboelectricity of the embedding substrates (Supplementary Table 4). Accordingly, we assessed the ML intensity of SrF_2:Pr^{3+} particles embedded in a series of polymer substrates (Fig. 4a). The results show that SrF_2:Pr^{3+}@polydimethylsiloxane (PDMS) presented the strongest ML as PDMS has the best negative triboelectricity than ER (epoxy resin), PU (polyurethane) and SG (silicon gel), consistent with the previously reported results (Supplementary Table 4). The above observations indicate that the triboelectric effect is also responsible for the ML from SrF_2:Pr^{3+}. The conclusion was further corroborated by green-emitting SrF_2:Tb^{3+} (Fig. 4a).

To gain insight into the trap-controlled ML mechanism after X-ray charging, we measured the PL (λ_{ex} = 440 nm, λ_{em} = 488 nm) and ML decay curves of SrF_2:0.5%Pr^{3+} (Supplementary Fig. 34). The results reveal that the duration time of ML is three orders of magnitude larger than that of PL. The observation supports the trap-controlled nature of the ML behavior, which involves the release and migration of charge carriers, thus taking a significantly longer time than PL (Supplementary Fig. 35). In line with the mechanically induced release of trap carriers, a transient enhancement of emission was detected at the PersL stage upon stimulation of external force (Fig. 4b). After repeated force stimulation, a notable dimming in PersL occurred at the location where the force was applied along with a significant decrease in the TL intensity (Figs. 4c, d). At the same time, the ML intensity constantly decreased. These results indicated that the PersL and ML originated from the same trapped charge carriers that can be released by both heat and force.

To shed more light on the multi-stimulated luminescence, the trapped charge carriers were adjusted by regulating the X-ray dose. With the increase of charging time, the ML intensified gradually (Fig. 4e). The observation is as anticipated due to the increased population in trap states, as confirmed by TL measurement (Supplementary Fig. 36). After performing the integral calculation, we clearly demonstrated the positive correlation of ML and TL intensities (Fig. 4f). As PersL is also closely related to TL, it is not difficult to understand that the stronger the PersL, the stronger the ML typically is (Supplementary Figs. 37 and 38). These observations provided additional evidence that the PersL and ML originated from the same trapped charge carriers. According to the TL spectra, we determined continuously distributed traps (Supplementary Figs. 39 and 40). The XRD pattern of SrF_2:Pr^{3+} was essentially unchanged upon exposure to X-ray (Supplementary Fig. 41), suggesting that the traps of SrF_2:Pr^{3+} were not due to the macro-structural change. We thus ascribe the trap states to intrinsic defects resulting from aliovalent doping. Our theoretical calculations (Supplementary Fig. 42 and Table 5 and Note 1) suggest that the substitution of two Pr^{3+} ions for two Sr^{2+} sites most

https://doi.org/10.1038/s41467-025-61522-6

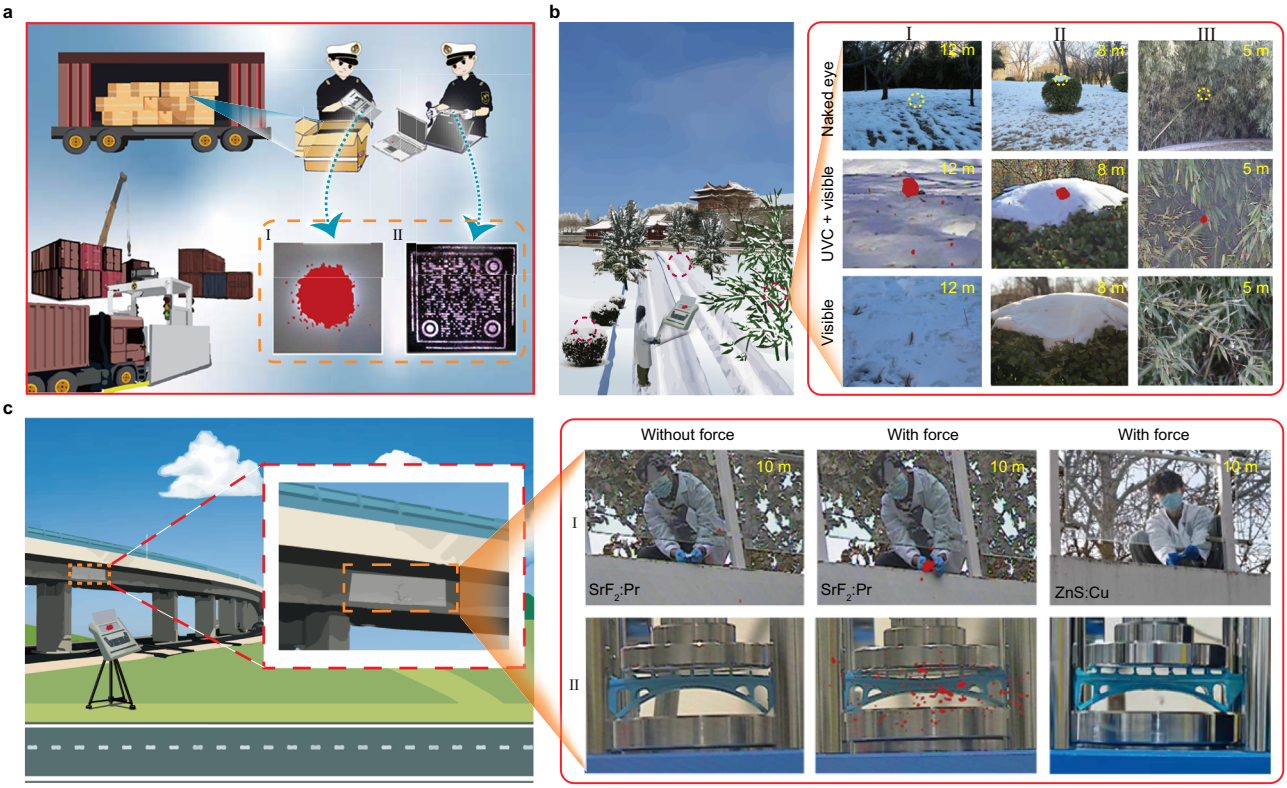

Fig. 5 | Optical imaging through far-UVC emission of $SrF_2:Pr^{3+}$. **a** Customs inspection. I and II show the photographs of $SrF_2:Pr^{3+}$ coated on the surface of goods after X-ray inspections, captured by collecting the UVC and visible emissions, respectively. **b** Solar-blind marking. The right panel presents the images of different complex scenarios that contain the $SrF_2:Pr^{3+}$ tablets, captured by using the visible or UVC+visible channel of a solar blind camera. **c** Structural health monitoring. The right panel shows the photographs of $SrF_2:Pr^{3+}$@polydimethylsiloxane and $ZnS:Cu^{2+}$@polydimethylsiloxane films, as well as $SrF_2:Pr^{3+}$@photopolymer resin and $ZnS:Cu^{2+}$@photopolymer resin under force stimulation by using the visible or UVC+visible channel of s solar blind camera.

likely occurred, resulting in one consequent Sr^{2+} vacancy. Moreover, fluorine vacancies and interstitials were expected to be generated in the fluorides under X-ray irradiation according to previous reports. Therefore, there were abundant defects in $SrF_2:Pr^{3+}$ to trap charge carriers[64–66].

Far-UVC emission for solar-blind imaging

We designed a quick response (QR) code made of SrF_2:0.5%Pr^{3+} and put it on the surface of high-valued goods. During X-ray inspections, the QR code was charged. After inspections, the QR code emitted both UVC and visible PersL that could be recorded separately by solar-blind and common cameras (Fig. 5a), providing a dual-layer anti-counterfeiting verification. Furthermore, even if the QR code's PersL diminished over time, the QR code could still be captured by a typical smartphone under mechanical stimulation (Supplementary Fig. 43). By incorporating such a unique QR code on product packaging, counterfeiting and illegal transportation can be prevented to a great extent.

Another important application for the UVC emission of $SrF_2:Pr^{3+}$ is high contrast marking. We prepared a series of $SrF_2:Pr^{3+}$ tablets with a diameter of 13 mm (Supplementary Fig. 44). As the samples are visually small and white, they are almost imperceptible to the naked eyes when placed in complex backgrounds such as in bamboo forests, holly bushes or snow. However, the positions of $SrF_2:Pr^{3+}$ tablets can be clearly identified by using a solar blind camera to capture the UVC PersL signal (Fig. 5b). We further constructed an array by mixing $SrF_2:Pr^{3+}$@PDMS with SrF_2@PDMS (Supplementary Fig. 45). After X-ray irradiation, the pattern 'Pr' was captured using the combined UVC and visible channel of solar blind camera. This method enables advanced marking techniques.

Health monitoring of engineering structures such as bridges and buildings is important for preventing structural failures that can lead to major disasters and economic losses. $SrF_2:Pr^{3+}$ holds important value for remote and real-time structural monitoring. We simulated two scenarios to illustrate the superiority of UVC photons. One involved directly pulling the $SrF_2:Pr^{3+}$@PDMS film coated on the surface of a real bridge (Fig. 5c-I), while the other involved compressing the $SrF_2:Pr^{3+}$@PDMS film coated on the surface of a 3D-printed bridge model (Fig. 5c-II). When external force was applied to the $SrF_2:Pr^{3+}$@PDMS film, the UVC emission was clearly captured in high contrast even in a bright environment. In this way, structural damage to the building, such as cracks, could be promptly collected and warned to prevent accidents and ensure safety. As a control experiment, we also employed the well-established $ZnS:Cu^{2+}$ with visible emission to replace $SrF_2:Pr^{3+}$ for the above demonstrations. Expectedly, no green ML could be observed due to the strong interference of background light, including intense outdoor sunlight and indoor lighting sources, although super bright ML was observed in dark environments (Supplementary Fig. 46). Considering the remarkable anti-interference capability of UVC photons, our samples are expected to unlock more applications such as emergency rescue (Supplementary Fig. 47). As the multi-stimulated luminescence can be substantially tuned across the full spectrum by doping different lanthanides, these materials also hold significant promise for information security and other advanced applications (Supplementary Figs. 48–51 and Note 2).

Discussion

In summary, we establish a set of design principles for far-UVC luminescence. Under the guidance of these principles, we develop a class of $SrF_2:Pr^{3+}$ crystals and realize unprecedented far-UVC ML at ≈222 nm through the inter-configurational $4f5d \rightarrow 4f^2$ transition of Pr^{3+}. By careful selection of dopant luminescent centers, including Ce^{3+}, Pr^{3+},

Nd^{3+}, Sm^{3+}, $Eu^{2+,3+}$, Gd^{3+}, Tb^{3+}, Dy^{3+}, Ho^{3+}, Er^{3+}, Tm^{3+} and Yb^{3+}, we further achieve tunable ML over the whole spectral range from 200 to 1700 nm, the widest emission wavelength span in a single host. Moreover, these materials can trap charge carriers following X-ray irradiation, giving rise to bright emissions by thermal and mechanical stimulations. The advances in these lanthanides-doped SrF_2 have enabled promising applications encompassing high-contrast imaging and structural health monitoring in bright and complex environments.

Methods

Materials

The chemicals include SrF_2 (99.99%, Aladdin), Pr_6O_{11} (99.99%, Aladdin), CeO_2 (99.9%, Aladdin), Gd_2O_3 (99.99%, Aladdin), Tb_4O_7 (99.9%, Aladdin), Dy_2O_3 (99.9%, Aladdin), Eu_2O_3 (99.99%, Aladdin), Sm_2O_3 (99.99%, Aladdin), Tm_2O_3 (99.9%, Aladdin), Nd_2O_3 (99.99%, Aladdin), Yb_2O_3 (99.99%, Aladdin), Ho_2O_3 (99.99%, Aladdin), Er_2O_3 (99.99%, Aladdin), NH_4F (99.99%, Aladdin), polyethylene terephthalate (PET, Deli 3816 plastic packaging film), PDMS (Sylgard 184, Dow Corning), ER (Shenzhen midisha composite material Co., Ltd), PU (Shenzhen huiruide technology co., Ltd) and SG (Shenzhen huiruide technology co., Ltd). Note that the commercial $ZnS:Cu^{2+}$ powder was directly purchased online (https://item.taobao.com/item.htm?id=683193241181).

Synthesis

Synthesis of $SrF_2:Pr^{3+}$ powder. The SrF_2 and Pr_6O_{11} were weighed according to the stoichiometric ratio. Next, the weighed powders were ground thoroughly for 30 min, followed by another 30-min grinding after adding sufficient NH_4F. Subsequently, the mixtures were sintered at 900 °C in an air environment for 2 h to obtain the final products. For the rest of the powder samples, the preparation procedures are similar to $SrF_2:Pr^{3+}$, except that the raw material of Pr_6O_{11} should be replaced by the corresponding rare earth oxides.

Synthesis of soft mechanoluminescent films. 0.3 g of $SrF_2:Pr^{3+}$ powder, 0.09 g of UV curing agent and 10 mL of ethyl alcohol were added to a centrifuge tube and ultrasonically treated for 30 min to form a homogeneous mixture. The mixture was then immediately poured into a 3*3 cm^2 mold placed on a PET film. The mechanoluminescent film was successfully obtained by evaporating the alcohol in a drying oven.

Synthesis of $SrF_2:Pr^{3+}$@PDMS composite. The $SrF_2:Pr^{3+}$ (or $SrF_2:Tb^{3+}$) powders were mixed with the PDMS precursor and curing agent in a 20 ml centrifuge tube. The mass ratio of $SrF_2:Pr^{3+}$ (or $SrF_2:Tb^{3+}$) powders, PDMS precursor and curing agent was fixed to 5.5:10:1. Thereafter, the above mixture was stirred for 20 min. Finally, it was poured into an acrylic sheet mold with a length of 50 mm and a width of 10 mm, and cured at 70 °C for 2 h to collect the target composite.

Synthesis of $SrF_2:Pr^{3+}$@ER composite. Initially, the $SrF_2:Pr^{3+}$ (or $SrF_2:Tb^{3+}$) powders were mixed with the ER precursor and curing agent in a 20 ml centrifuge tube. The mass ratio of $SrF_2:Pr^{3+}$ (or $SrF_2:Tb^{3+}$) powders, SG precursor and curing agent was maintained at 2:3:1. Next, the above mixture was stirred for 20 min. Finally, it was poured into a silica gel grinder with a diameter of 8 mm and cured at 60 °C for 2 h to obtain the final composite.

Synthesis of $SrF_2:Pr^{3+}$@SG composites. The $SrF_2:Pr^{3+}$ (or $SrF_2:Tb^{3+}$) powders were mixed with the SG precursor and curing agent in a 20 ml centrifuge tube. The mass ratio of $SrF_2:Pr^{3+}$ (or $SrF_2:Tb^{3+}$) powders, SG precursor and curing agent was set to 5.5:10:1. After that, the above mixture was stirred for 20 min. In the end, it was poured into an acrylic mold with a length of 50 mm and a width of 10 mm, and cured at 70 °C for 6 h to obtain the sample.

Synthesis of $SrF_2:Pr^{3+}$@PU composites. Firstly, the $SrF_2:Pr^{3+}$ (or $SrF_2:Tb^{3+}$) powders were mixed with the PU precursor and curing agent in a 20 ml centrifuge tube. The mass ratio of $SrF_2:Pr^{3+}$ (or $SrF_2:Tb^{3+}$) powders, PU precursor A and PU precursor B was kept at 1:1:1. Subsequently, the above mixture was stirred for 20 min. Finally, it was poured into an acrylic mold with a length of 50 mm and a width of 10 mm, and cured at 70 °C for 2 h to obtain the product.

Material characterization

The crystal structure of samples was characterized by XRD (Bruker Optics, Cu-*Kα*). The valence states of samples were determined using XPS (Thermo Fisher Scientific, ESCALAB 250Xi; resolution: 0.45 eV). The morphological and elemental composition analyses of samples were performed using an SEM instrument (FEI Nova Nano SEM450) equipped with an EDS detector. The fine lattice structures of samples were observed using HR-TEM (JEOL-2100Plus). The Raman spectrum of samples was collected with a Raman spectrometer (Horiba Jobin Yvon, HR Evolution). The PFM measurements were conducted using a scanning probe microscope (Nanoscope V Multimode 8) from Bruker Corporation.

Optical measurement

An X-ray radiator (Dandong Tongda Science and Technology Co., Ltd., CT; 30 mA, 40 kV, W target) was used as the excitation source. The PersL and ML spectra of samples were obtained using a fiber optic spectrometer (QE65-pro and Maya2000-pro, Ocean Optics, 200–950 nm; NIR-Quest, Ocean Optics, 950–1700 nm). The ML performance of samples was quantitatively assessed using a custom apparatus consisting of a gravity-sensitive device, a fiber optic spectrometer, a programmable motion platform and a sample mounting plate. The mechanoluminescent powder was placed in the upper part of a mortar. The stress sensing device was placed on a programmable movable platform. A transparent quartz tube was fixed on the displacement platform, and the external force was applied to the sample through the displacement platform.

The ML reproducibility of samples was assessed quantitatively using a custom-built apparatus consisting of digital push-pull equipment, a fiber-optic spectrometer, a programmable mobile platform, and a sample-fixing plate. The mechanoluminescent PET film was pasted onto a quartz glass sheet. On one side, the digital push-pull instrument equipped with a metal attachment was fixed on a programmable mobile platform. The digital push-pull equipment controlled the applied force, and the ML signal was collected using the fiber-optic spectrometer. The ML Photographs of samples were taken using a digital camera (Canon 5D). The authors affirm that human research participants provided informed consent for publication of the images in Fig. 5 and Supplementary Fig. 47.

ML lifetime measurement

The $SrF_2:Pr^{3+}$@PDMS film was stretched by a universal testing machine (Stretching rate: 15 mm/sec for 5 mm). The ML signal was received by a photomultiplier tube (R928, Hamamatsu, Japan) at the moment the stretching was immediately halted. The ML signal was then read by a high resistance/low current electrostatic meter (6500/6430 series, Keithley) through a voltage amplifier.

PL lifetime measurement

A tunable laser (OPOTEK, Compact OPO Laser-Opolette Series, frequency: 20 Hz, pulse width: 6 ms) was used as the excitation source. The PL signal was collected by a photomultiplier tube (R928, Hamamatsu, Japan) coupled to an oscilloscope (MDO32, Tektronix).

First-principles calculation

First-principles density functional theory (DFT) calculations were performed using the Vienna Ab initio Simulation Package[67–69]. The projector augmented-wave (PAW) potential was adopted to describe the core electrons, and the valence electrons were described by plane-wave basis with an energy cut-off of 500 eV[70,71]. The exchange-correlation functional adopted the generalized gradient approximation in the Perdew-Burke-Ernzerhof form (GGA-PBE)[72]. The convergence criteria were 10^{-7} eV for the self-consistent energy calculation

and 0.01 eV/Å for the Hellmann-Feynman force in the geometric optimization. The Brillouin zone was sampled using Monkhorst-Pack scheme with a *k*-point density of $2\pi \times 0.03$ Å^{-1}. The atomic coordinates of the optimized computational models are provided in the Source Data file as data related to Supplementary Fig. 42.

Data availability

The data supporting the findings of this study are available within the paper and its Supplementary Information files. Should any raw data files be needed in another format they are available from the corresponding authors upon request. Source data are provided with this paper.

References

1. Chen, T. & Yan, D. Full-color, time-valve controllable and Janus-type long-persistent luminescence from all-inorganic halide perovskites. *Nat. Commun.* **15**, 5281 (2024).
2. Hariyani, S., Sójka, M., Setlur, A. & Brgoch, J. A guide to comprehensive phosphor discovery for solid-state lighting. *Nat. Rev. Mater.* **8**, 759–775 (2023).
3. Zhuang, Y. & Xie, R. J. Mechanoluminescence rebrightening the prospects of stress sensing: a review. *Adv. Mater.* **33**, 2005925 (2021).
4. Lyu, T. & Dorenbos, P. Charge carrier trapping management in Bi^{3+} and lanthanides doped Li (Sc, Lu) GeO_4 for X-ray imaging, anti-counterfeiting, and force recording. *Appl. Phys. Rev.* **11**, 011415 (2024).
5. Wang, Y. et al. In vivo ultrasound-induced luminescence molecular imaging. *Nat. Photonics* **18**, 334–343 (2024).
6. Zhou, X. et al. Interplay of defect levels and rare earth emission centers in multimode luminescent phosphors. *Nat. Commun.* **13**, 7589 (2022).
7. Chun, F. et al. Multicolour stretchable perovskite electroluminescent devices for user-interactive displays. *Nat. Photonics* **18**, 856–863 (2024).
8. Wang, X. et al. Organic phosphors with bright triplet excitons for efficient X-ray-excited luminescence. *Nat. Photonics* **15**, 187–192 (2021).
9. Xu, J. & Tanabe, S. Persistent luminescence instead of phosphorescence: history, mechanism, and perspective. *J. Lumin.* **205**, 581–620 (2019).
10. Lyu, T. & Dorenbos, P. Liquid nitrogen temperature to 700 K Bi^{3+} thermoluminescence: toward wide temperature-range light dosimeters for versatile anti-counterfeiting, information storage, and X-ray imaging. *Appl. Phys. Rev.* **11**, 041417 (2024).
11. Chang, S. et al. Mechanoluminescent functional devices: developments, applications and prospects. *Nano Energy* **122**, 109325 (2024).
12. Listyawan, M. A. et al. Magnetically driven powerless lighting device with kirigami structured magneto-mechanoluminescence composite. *Adv. Sci.* **10**, 2207722 (2023).
13. Luo, J. et al. Modulating smart mechanoluminescent phosphors for multistimuli responsive optical wood. *Adv. Sci.* **11**, 2305066 (2024).
14. Huang, Z. et al. Smart mechanoluminescent phosphors:a review of strontium-aluminate-based materials, properties, and their advanced application technologies. *Adv. Sci.* **10**, 2204925 (2023).
15. Wang, W., Wang, S., Gu, Y., Zhou, J. & Zhang, J. Contact-separation-induced self-recoverable mechanoluminescence of CaF_2:Tb^{3+}/PDMS elastomer. *Nat. Commun.* **15**, 2014 (2024).
16. Pan, X. et al. Quantifying the interfacial triboelectricity in inorganic-organic composite mechanoluminescent materials. *Nat. Commun.* **15**, 2673 (2024).
17. Zhang, J. C., Wang, X., Marriott, G. & Xu, C. N. Trap-controlled mechanoluminescent materials. *Prog. Mater. Sci.* **103**, 678–742 (2019).
18. Hou, T. et al. An ultra thin, bright, and sensitive interactive tactile display based on organic mechanoluminescence for dual-mode handwriting identification. *InfoMat* **6**, 12523 (2024).
19. Li, C. et al. Ultrasensitive and robust mechanoluminescent living composites. *Sci. Adv.* **9**, eadi8643 (2023).
20. Petit, R. R., Michels, S. E., Feng, A. & Smet, P. F. Adding memory to pressure-sensitive phosphors. *Light Sci. Appl.* **8**, 124 (2019).
21. Jeong, S. M. et al. Bright, wind-driven white mechanoluminescence from zinc sulphide microparticles embedded in a polydimethyl siloxane elastomer. *Energy Environ. Sci.* **7**, 3338–3346 (2014).
22. Tang, Y. et al. Dynamic multicolor emissions of multimodal phosphors by Mn^{2+} trace doping in self-activated $CaGa_4O_7$. *Nat. Commun.* **15**, 3209 (2024).
23. Yang, J. C. et al. Electronic skin: recent progress and future prospects for skin-attachable devices for health monitoring, robotics, and prosthetics. *Adv. Mater.* **31**, 1904765 (2019).
24. Zhou, B. et al. Mechanoluminescent-triboelectric bimodal sensors for self-powered sensing and intelligent control. *Nano Micro Lett.* **15**, 72 (2023).
25. Qin, S. et al. Self-recoverable, highly repeatable, and thermally stable mechanoluminescence for dual-mode information storage and photonic skin applications. *Adv. Funct. Mater.* **34**, 2401535 (2024).
26. Jeong, H. I. et al. Super elastic and negative triboelectric polymer matrix for high performance mechanoluminescent platforms. *Nat. Commun.* **16**, 854 (2025).
27. Ding, Y., So, B., Cao, J. & Wondraczek, L. Ultrasound-induced mechanoluminescence and optical thermometry toward stimulus-responsive materials with simultaneous trigger response and read-out functions. *Adv. Sci.* **9**, 2201631 (2022).
28. Xu, C. N., Watanabe, T., Akiyama, M. & Zheng, X. Artificial skin to sense mechanical stress by visible light emission. *Appl. Phys. Lett.* **74**, 1236–1238 (1999).
29. Xu, C. N., Watanabe, T., Akiyama, M. & Zheng, X. G. Direct view of stress distribution in solid by mechanoluminescence. *Appl. Phys. Lett.* **74**, 2414–2416 (1999).
30. Chen, C. et al. Creating visible-to-near-infrared mechanoluminescence in mixed-anion compounds $SrZn_2S_2O$ and SrZnSO. *Nano Energy* **68**, 104329 (2020).
31. Wang, C. et al. Enabling multimodal luminescence in a single nanoparticle for X-ray imaging encryption and anticounterfeiting. *Nano Lett.* **24**, 9691–9699 (2024).
32. Chen, B., Zhang, X. & Wang, F. Expanding the toolbox of inorganic mechanoluminescence materials. *Acc. Mater. Res.* **2**, 364–373 (2021).
33. Liu, S. et al. Near-infrared mechanoluminescence of Cr^{3+} doped gallate spinel and magnetoplumbite smart materials. *Adv. Funct. Mater.* **33**, 2209275 (2023).
34. Wang, H. et al. Oscillatory mechanoluminescence of Mn^{2+}-doped SrZnOS in dynamic response to rapid compression. *Nat. Commun.* **16**, 548 (2025).
35. Zhou, S., Cheng, Y., Xu, J., Lin, H. & Wang, Y. Ratiometric mechanoluminescence of double-activator doped phosphatic phosphors: color-resolved visualization of stress-sensing and quantified evaluation for sensing performance. *Adv. Funct. Mater.* **32**, 2208919 (2022).
36. Yang, Y. L. et al. Time-resolved bright red to cyan color tunable mechanoluminescence from CaZnOS:Bi^{3+}, Mn^{2+} for anti-counterfeiting device and stress sensor. *Adv. Opt. Mater.* **9**, 2100668 (2021).
37. Xiong, P., Peng, M. & Yang, Z. Near-infrared mechanoluminescence crystals: a review. *iScience* **24**, 101944 (2021).
38. Wang, X. et al. Piezophotonic effect based on mechanoluminescent materials for advanced flexible optoelectronic applications. *Nano Energy* **55**, 389–400 (2019).
39. Du, Y. et al. Mechanically excited multicolor luminescence in lanthanide ions. *Adv. Mater.* **31**, 1807062 (2019).
40. Li, L., Wondraczek, L., Peng, M., Ma, Z. & Zou, B. Force-induced 1540 nm luminescence: role of piezotronic effect in energy transfer process for mechanoluminescence. *Nano Energy* **69**, 104413 (2020).
41. Yang, Y. et al. Fluorescence-amplified nanocrystals in the second near-infrared window for in vivo real-time dynamic multiplexed imaging. *Nat. Nanotechnol.* **18**, 1195–1204 (2023).

42. Yang, Y., Jiang, Q. & Zhang, F. Nanocrystals for deep-tissue in vivo luminescence imaging in the near-infrared region. *Chem. Rev.* **124**, 554–628 (2023).
43. Yang, X. et al. Energy focusing reinforced narrowband ultraviolet-b mechanoluminescence for bright-field stress visualization. *J. Mater. Chem. C.* **11**, 6912–6919 (2023).
44. Li, P. et al. Mechanically induced photons from ultraviolet-c to near-infrared in Tm^{3+}-doped MgF_2. *Opt. Express* **31**, 22396–22404 (2023).
45. Li, L. et al. Ultraviolet-c mechanoluminescence from $NaYF_4$:Pr^{3+}. *Appl. Phys. Lett.* **124**, 101108 (2024).
46. Li, H., Yang, Y., Li, P., Peng, D. & Li, L. Force-induced ultraviolet c luminescence of Pr^{3+}-doped $Sr_2P_2O_7$ for X-ray dosimetry. *Adv. Mater.* **36**, 2411804 (2024).
47. Zhang, Y. et al. Long-persistent far-uvc light emission in Pr^{3+}-doped $Sr_2P_2O_7$ phosphor for microbial sterilization. *Inorg. Chem. Front.* **10**, 5958–5968 (2023).
48. Wang, X. & Mao, Y. Recent advances in Pr^{3+}-activated persistent phosphors. *J. Mater. Chem. C.* **10**, 3626–3646 (2022).
49. Kück, S., Sokólska, I., Henke, M., Scheffler, T. & Osiac, E. Emission and excitation characteristics and internal quantum efficiencies of vacuum-ultraviolet excited Pr^{3+}-doped fluoride compounds. *Phys. Rev. B Condens. Matter Mater. Phys.* **71**, 165112 (2005).
50. Kück, S. & Sokólska, I. Observation of photon cascade emission in Pr^{3+}-doped LuF_3 and $BaMgF_4$. *Chem. Phys. Lett.* **364**, 273–278 (2002).
51. Srivastava, A. Aspects of Pr^{3+} luminescence in solids. *J. Lumin.* **169**, 445–449 (2016).
52. Li, L. et al. Pr^{3+}-based visible-to-ultraviolet upconversion. a minireview. *Adv. Phys. Res.* **4**, 2400097 (2025).
53. Srivastava, A. & Beers, W. Luminescence of Pr^{3+} in $SrAl_{12}O_{19}$: observation of two photon luminescence in oxide lattice. *J. Lumin.* **71**, 285–290 (1997).
54. Dawei, W., Shihua, H., Fangtian, Y., Shiqun, Q. & Guobin, Z. Temperature-dependent emission of Pr^{3+}-doped LaB_3O_6 under vacuum ultraviolet excitation. *J. Rare Earths* **25**, 4 (2007).
55. Lawson, J. K. & Payne, S. A. Excited-state absorption of Pr^{3+}-doped fluoride crystals. *Opt. Mater.* **2**, 225–232 (1993).
56. Karimi, M., Hesaraki, S. & Nezafati, N. In vitro biodegradability-bioactivity-biocompatibility and antibacterial properties of SrF_2 nanoparticles synthesized by one-pot and eco-friendly method based on ternary strontium chloride-choline chloride-water deep eutectic system. *Ceram. Int.* **44**, 12877–12885 (2018).
57. Alcalá, R., González, J. C. & Alonso, P. Charge change processes of 3d-ions in doped SrF_2. *J. Lumin.* **26**, 141–150 (1981).
58. Beaumont, J., Hayes, W., Kirk, D. & Summers, G. An investigation of trapped holes and trapped excitons in alkaline earth fluorides. *Proc. R. Soc. Lond. A Math. Phys. Sci.* **315**, 69–97 (1970).
59. Liang, Y. et al. Migrating photon avalanche in different emitters at the nanoscale enables 46th-order optical nonlinearity. *Nat. Nanotechnol.* **17**, 524–530 (2022).
60. Suo, H. et al. Excitation-mode-selective emission through multi-excitonic states in a double perovskite single crystal. *Light Sci. Appl.* **14**, 21 (2025).
61. Wu, S. et al. Single Tb^{3+} ion doped ratiometric mechanoluminescence for tunable stress visualization. *Chem Eng. J.* **469**, 143961 (2023).
62. Tian, B. et al. Stress-induced color manipulation of mechanoluminescent elastomer for visualized mechanics sensing. *Nano Energy* **83**, 105860 (2021).
63. Zhang, J. C. et al. An intense elastico-mechanoluminescence material CaZnOS:Mn^{2+} for sensing and imaging multiple mechanical stresses. *Opt. Express* **21**, 12976–12986 (2013).
64. Lei, L. et al. Dual heterogeneous interfaces enhance X-ray excited persistent luminescence for low-dose 3D imaging. *Nat. Commun.* **15**, 1140 (2024).
65. Ou, X. et al. High-resolution X-ray luminescence extension imaging. *Nature* **590**, 410–415 (2021).
66. Peng, S. C. et al. Mechano-luminescence behavior of lanthanide-doped fluoride nanocrystals for three-dimensional stress imaging. *Acs Nano.* **17**, 9543–9551 (2023).
67. Jones, R. O. Density functional theory: its origins, rise to prominence, and future. *Rev. Mod. Phys.* **87**, 897 (2015).
68. Kresse, G. & Furthmüller, J. Efficient iterative schemes for ab initio total-energy calculations using a plane-wave basis set. *Phys. Rev. B***54**, 11169 (1996).
69. Kresse, G. & Hafner, J. Ab initio molecular-dynamics simulation of the liquid-metal-amorphous-semiconductor transition in germanium. *Phys. Rev. B.* **49**, 14251 (1994).
70. Blöchl, P. E. Projector augmented-wave method. *Phys. Rev. B.* **50**, 17953 (1994).
71. Kresse, G. & Joubert, D. From ultrasoft pseudopotentials to the projector augmented-wave method. *Phys. Rev. B.* **59**, 1758 (1999).
72. Perdew, J. et al. Generalized gradient approximation made simple. *Phys. Rev. Lett.* **77**, 3865 (1996).

Acknowledgements

L. Li acknowledges the National Natural Science Foundation of China (12474401), the Science and Technology Project of Hebei Education Department (BJK2024084), and the Hong Kong Scholars Program (XJ2024034). Y. Yang acknowledges the National Natural Science Foundation of China (12374373) and the Natural Science Interdisciplinary Research Program of Hebei University (No. DXK202301). D. Peng acknowledges the Key-Area Research and Development Program of Guangdong Province (2024B0101080001), the Natural Science Foundation of China (62275170), the Guangdong Provincial Science Fund for Distinguished Young Scholars (2022B1515020054), Scientific Research Foundation as Phase III construction of high-level University 2035 plan (0000050101) and the proof-of-concept project of Shenzhen University (000003011313), as well as Medical-Engineering Interdisciplinary Research Foundation of Shenzhen University (2023YG031). F. W. acknowledges the Research Grants Council of Hong Kong for a General Research Fund (No. 11211922).

Author contributions

L.L., D.P., F.W., and Y.Y. conceived the concept and supervised the project. C.C. carried out the sample synthesis and optical measurements with help from L.L., H.L., T.Li., P.L., W.Z., L.Z., S.F., X.F., and H.Z. X.L. performed the theoretical calculation. J.Q. participated in the discussion of physical mechanisms. L.L. and C.C. wrote the original manuscript. L.L., C.C., and F.W. revised the manuscript. All authors contributed to the manuscript.

Competing interests

The authors declare no competing interests.

Additional information

Supplementary information The online version contains supplementary material available at https://doi.org/10.1038/s41467-025-61522-6.

Correspondence and requests for materials should be addressed to Leipeng Li, Dengfeng Peng, Feng Wang or Yanmin Yang.

Peer review information *Nature Communications* thanks Xiao-Jun Wang, and the other, anonymous, reviewer(s) for their contribution to the peer review of this work. A peer review file is available.